
Experimental Analysis of Millimeter-wave Channels Based on a Virtual Cubic Antenna Array VNA Based System.

- Master's Thesis -



AALBORG UNIVERSITY
UNIVERSITY OF CASSINO AND SOUTHERN LAZIO



-ALLAN WAINAINA MBUGUA-

Wireless Communication Systems

Msc. Telecommunications Engineering



AALBORG UNIVERSITY
DENMARK

Department of Electronic Systems

Wireless Communication Systems
Fredrik Bajers Vej 7B, 9220 Aalborg Ø
Phone +45 9940 8600
<http://www.es.aau.dk>



Department of Electrical and Information Engineering

Msc. Telecommunications Engineering
Via Gaetano di Biaso 43, 03043 Cassino (FR), Italy
<http://www.uniclam.it/siti/dipartimenti/diei.aspx>

Title:

Experimental Analysis of millimeter-wave channels
based on a virtual cubic antenna array VNA based system

Project period:

February 3rd 2017 - June 8th 2017

Participant:

Allan Wainaina Mbugua

Supervisors:

Dr. Wei Fan
Yilin Ji

Report pages: 35

Completed: 8-06-2017

ABSTRACT

In this thesis we carry out measurement campaigns in an indoor environment with an aim of investigating the channel characteristics of millimeter waves particularly for the band 26 - 30 GHz. The channel is sampled massively in space by use of a virtual uniform cubic array (UCuA) and a vector network analyzer (VNA).

We begin by automating the measurement system, with an aim of achieving high repeatability, reliability and accuracy. Measurement campaigns are then carried out in a moderately furnished room for the line of sight (LOS) and obstructed line of sight (OLOS) scenarios.

The angle of arrival (AOA) of the multipath components (MPC) are obtained by classical beamforming for the azimuth and elevation planes. The power angle delay profile (PADP) showed that the most significant MPC were due to specular reflection for the LOS scenario. In the OLOS scenario diffuse scattering is observed which was highly influenced by the construction of the obstructor.

The identified MPC are related to the room geometry, and the effect of furniture on propagation investigated. A change in the wall reflectivity in particular had a significant effect on the tail of the power delay profile (PDP) and the root mean square (RMS) delay spread.

The measurement system was robust and highly repeatable as shown in the results which provides us with a tool for further analysis of other millimeter wave bands.

ACKNOWLEDGEMENTS

I would like express my heartfelt gratitude to my supervisor Dr. Wei Fan and my co-supervisor Yilin Ji for their immense support, availability, guidance and for believing in me throughout the project. Dr. Wei and Yilin gave me a new perspective on how to solve research problems.

I would also like to thank my supervisor, Dr. Luca Venturino from University of Cassino and Southern Lazio, Italy for his oversight during my project.

Kim Olesen greatly guided me in the measurement, his support and expertise in channel sounding made this project a success. Moreover he brought the *hygge* in the lab.

I would like to also thank Stanislav Zhekov, who went out of his way to share his experience with the linear positioning stages, his advice on the antenna that he developed which was used in the measurement campaigns and for his constant encouragement.

Furthermore I would like to thank Fengchun Zhan, Johannes Hejselbæk whose insights were invaluable.

The entire APNet team at the Department of Electronic systems in Aalborg University has been very supportive and the conducive work environment certainly contributed to the success of this project.

I would like also to thank Forid Gobuzi who spared his time to introduce me to Latex, Daniele Petrocelli and Lawrence Ngugi for their guidance during my master's in Italy.

Finally I would like to thank my family: My parents, Mr. and Mrs. Mbugua, my siblings Wangari Nyaga, Munene Nyaga and Karera Mbugua for always being there in every step of the journey. My late grandparents, Wamucami and Karoki wa Ndinye, who passed on during my stay abroad paid the ultimate price to have a liberated Kenya and this work is as a result of their sweat and tears. I will forever be grateful for their sacrifice.

LIST OF ACRONYMS AND ABBREVIATIONS

5G	fifth generation
AOA	angle of arrival
BS	base station
CIR	channel impulse response
DUT	device under test
FSPL	free space path loss
IDFT	inverse discrete fourier transform
IF	intermediate frequency
IFFT	inverse fast fourier transform
ISI	inter symbol interference
LO	local oscillator
LOS	line of sight
LTI	linear time invariant
Mcps	mega-chips per second
MS	mobile station
MIMO	multiple-input multiple-output
MPC	multipath components
MUSIC	multiple signal classification
OFDM	orthogonal frequency division multiplexing
OLOS	obstructed line of sight
PADP	power angle delay profile
PC	personal computer
PDP	power delay profile
RF	radio frequency
Rx	receiver
RMS	root mean square
SAGE	space-alternating generalized expectation
SCPI	standard commands for programmable instruments
SIR	signal to interference ratio
SISO	single-input single-output
SIMO	single-input multiple-output
Tx	transmitter
TTL	transistor transistor logic
UCA	uniform circular array
UCuA	uniform cubic array
ULA	uniform linear array
URA	uniform rectangular array
UWB	ultra wideband
VNA	vector network analyzer
WLAN	wireless local area network

TABLE OF CONTENTS

Abstract	ii
Acknowledgements	iv
List of Acronyms and Abbreviations	vi
Table of contents	vi
List of Figures	vii
List of Tables	ix
Chapter 1 Introduction	1
1.1 Thesis Outline	2
1.2 Channel Sounding	2
1.3 Virtual Arrays for Channel sounding	3
1.4 Angle of Arrival Estimation	4
1.5 Indoor Propagation	4
1.6 Time Dispersion	4
Chapter 2 Channel Sounding and Measurement Setup	7
2.1 Measurement Setup	7
2.2 Virtual Antenna Array	9
2.3 Measurement Procedure	11
2.4 Measurement Scenario	13
Chapter 3 Results and Analysis	19
3.1 The Indoor Propagation Channel	19
3.2 Power Delay Profile	21
3.3 Fresnel Zone	21
3.4 Power Angle Delay Profile	22
3.5 RMS Delay Spread	28
3.6 Spatial Aliasing	29
Chapter 4 Conclusion and Future Work	31
4.1 Conclusion	31
4.2 Future Work	31
Bibliography	33

LIST OF FIGURES

- 2.1 Positioner Cartesian Coordinates Mapping. 10
- 2.2 Virtual uniform rectangular array (URA) geometry. 10
- 2.3 Virtual UCuA geometry. 11
- 2.4 Measurement Setup: radio frequency (RF) cables are in red. 12
- 2.5 Variation of phase and magnitude due to movement of the flex coaxial cable. 13
- 2.6 Antenna Location with respect to room geometry: All dimensions in mm. 14
- 2.7 Antenna Location with respect to room geometry, campaign 1: All dimensions in mm. 15
- 2.8 Room Photos: Measurement campaign 2 (LOS and OLOS). 16
- 2.9 Panorama view of the kitchen: Measurement campaign 1. 16
- 2.10 Room Photos: Co-Location Measurement (campaign 2), where d is the separation distance of the two antennas. 17

- 3.1 A comparison of the PDP for the two measurement campaigns 22
- 3.2 A comparison of the average PDP for the two measurement campaigns. 23
- 3.3 Propagation paths in relation to room geometry: All dimensions in mm. 24
- 3.4 PADP for measurement campaign 1 [3.4c,3.4d] and measurement campaign 2 [3.4a,3.4b]. 25
- 3.5 Elevation angle for the start, center and stop frequency, measurement campaign 2. 27
- 3.6 Simulated Antenna Array Response. 29

LIST OF TABLES

- 2.1 intermediate frequency (IF) bandwidth setting of the VNA and the corresponding sweep time. 8
- 2.2 Summary of various parameters 9
- 2.3 Antenna heights in meters: Measurement campaign 1 and 2. 14
- 2.4 Obstructor distance for measurement campaign 2, with an inter-element spacing of 0.4λ . . . 17
- 2.5 Obstructor distance for measurement campaign 1, with an inter-element spacing of 0.5λ . . . 18

- 3.1 Propagation paths and the corresponding power levels: LOS, measurement campaign 2. . . . 26
- 3.2 Propagation paths and the corresponding power levels: OLOS, measurement campaign 2. . . 26
- 3.3 RMS delay spread (σ_τ) and mean excess delay ($\bar{\tau}$) for different noise floor in the LOS and OLOS scenarios. 28

INTRODUCTION

With the increased demand for higher data rates, there has been a general consensus that the current mobile networks will not be able to meet future demand, and thus the need for the fifth generation (5G) mobile network. In order to achieve higher data rates, the 5G mobile networks will require more bandwidth, which lies in the millimeter-wave band that is largely unused [1]. Accurate characterization of the millimeter-wave band propagation channel is crucial in the proper design of the 5G networks.

Currently the millimeter wave band centered at 60 GHz has been researched widely and it is being used in IEEE 802.11ad for wireless local area network (WLAN). Oxygen absorption at 60 GHz, limits the radius of the cell and thus allowing frequency re-use and reduction of inter-user interference in different cells [2].

Researchers are currently focusing on other millimeter wave bands for example the 28 GHz, 38 GHz and 73 GHz, which will aid in achieving the "tactile internet" through reduction of latency to about 1 ms brought about by the increased bandwidth [3],[1]. It therefore becomes important to study the similarities and the differences of these bands for proper channel modelling.

Massive multiple-input multiple-output (MIMO) is going to be a key driver for the efficient utilization of the ultra wideband (UWB). Since the wavelength of millimeter-waves is small relative to the typical mobile terminals, the opportunity of implementation of a large number of antennas for a given area, both at the base station (BS) and mobile station (MS) readily presents itself, thus bringing the fruition of massive MIMO closer [4].

A large number of antenna elements will allow pencil beamforming to combat the effects of multipath and simultaneously permit spatial separation of mobile users, thus reducing signal to interference ratio (SIR). Moreover energy efficiency is expected to increase as base stations will focus their energy on specific users instead of broadcasting over a large area. The concept of frequency re-use will also be improved greatly as users will be spatially separated.

In this thesis the focus will be the investigation of the spatial temporal characteristics of the millimeter wave band centered at 28 GHz, using a virtual UCuA, and a VNA based channel sounder. The investigation of the multipaths is of particular importance for massive MIMO, since they can be viewed as parallel channels critical in boosting capacity [5].

1.1 Thesis Outline

This chapter gives an overview of channel sounding using a VNA and virtual antenna arrays. Chapter 2 outlines the automation of the measurement system, the measurement setup and the procedures carried out during the measurement campaigns. In chapter 3, the data collected in the measurement campaign is analyzed and the results are discussed. Chapter 4 gives a conclusion of the thesis as well as the future work, based on the data collected in the measurement campaigns.

1.2 Channel Sounding

The VNA, which is a swept spectrum method of channel sounding, works in the frequency domain and the temporal response can be recovered using the Fourier transform. The radio channel is considered as the device under test (DUT) which is linear time invariant (LTI) and the channel frequency response is obtained from the scattering matrix, where the phase and magnitude of the frequency band of interest are recorded. The propagation channel in this thesis is considered reciprocal.

The VNA provides a quite a simple method of channel sounding, with a high delay resolution, however, the penalty is increased measurement time [6]. This can be a limitation in cases where it is difficult to keep the channel static for an extended period of time, as the time to have "one snapshot", could be in the range of several hours. This was a bottleneck in the measurement campaigns conducted for this thesis, where measurements could only be carried out during weekends.

Channel sounding with a VNA has the disadvantage of limited range, due to the high path loss in millimeter waves and attenuation in the cables. The path loss is higher for millimeter waves as demonstrated by Friss formula in eq. 1.1. This implies that the higher the frequency the higher the path loss. The free space path loss (FSPL) is given as:

$$\text{FSPL} = 20 \log_{10} \left(\frac{4\pi f d}{c} \right) \quad (1.1)$$

where d is the distance between the transmitter (Tx) and receiver (Rx), f the frequency and c the speed of light.

However, for the measurement campaigns conducted here in, the size of the room justified the use of a VNA. Various researchers have improved the VNA channel sounding method, for example by use of external mixers and local oscillator (LO)/IF distribution unit in [7], where the author down converts the signal to a lower frequency to reduce signal loss in the cables. This was a technique employed also in [4].

In this case our measurements are carried out in a short range and thus the dynamic range of the system shown in fig 2.4 is sufficient to correctly characterize the channel thus it does not warrant the increase in complexity of the setup as in [7].

Dedicated channel sounders that work in the time domain though fast, have a limitation on the bandwidth that they can cover thus falling short of the UWB requirement that is a focus of this thesis [8].

Several other researchers have used sliding correlator channel sounders. For instance, [3] have a 400 mega-chips per second (Mcps) sliding correlator that they used to perform outdoor measurement campaigns at 28 GHz with a 2.3 ns delay resolution.

In [9] a custom channel sounder, that uses a spread spectrum signal with a bandwidth of 7 GHz was used for measurement campaign at 60 GHz, with a high gain directional Tx antenna.

1.3 Virtual Arrays for Channel sounding

Using linear positioning stages, virtual antenna arrays can be implemented as outlined in section 2.2.

The virtual UCuA, can be viewed as a stack of several layers of the URA, thus enabling resolution of angular information in the elevation and azimuth plane. In [10], a virtual UCuA is used, with simulations of a spherical and three orthogonal quadratic arrays at 60 GHz, showing the presence of fictitious angles in the last two arrays at -12 dB and -25 dB respectively below the main peak. The authors thus performed their channel measurement using a virtual UCuA, which from their simulation results had fictitious peaks below -50 dB from the main peak.

Other virtual arrays that are used in channel sounding include the uniform linear array (ULA) which is not able to resolve angle information for paths that are symmetric to the array line [4],[11]. Moreover the angle resolution in the endfire direction is poor. The URA, an improvement to the ULA is able to resolve angle information in the azimuth plane but has a poor resolution in the elevation plane. Another type of antenna array is the virtual uniform circular array (UCA), which has also been a choice in many measurement campaigns, owing to its ability to resolve angle information in the azimuth plane [4],[12],[13].

1.3.1 Advantages of Virtual Arrays

Virtual antenna arrays are very convenient for this measurement campaign as we only have one RF transceiver chain. This makes the system cost effective as well as simplifying the hardware set up with very simple calibration hence it becomes easy to perform channel sounding without having to manufacture and test antenna arrays, which can be time intensive.

Virtual arrays enable creation of antenna arrays that would otherwise have been very difficult or impossible to manufacture, for example the UCuA used in this measurement campaign. For virtual arrays only a modification of software is needed to reconfigure or modify the antenna array.

Virtual arrays do not have mutual coupling inherent in real antenna arrays [5],[33]. Mutual coupling in antenna arrays causes power loss hence the lack of it in our system is an advantage.

The antenna array aperture is only limited by the physical size of the linear positioning stages, thus very flexible.

Once the data is recorded, it can be combined in post-processing to form a different type of array geometry.

1.3.2 Disadvantages of Virtual Arrays

Virtual arrays have the disadvantage of long measurement time. In the measurement campaigns carried out we used approximately 25 hours with the virtual UCuA to record one "snapshot".

The long measurement time brings about the challenge of keeping the channel static for the period required to take one "snapshot".

Virtual antenna arrays are not applicable in linear time variant channels.

1.4 Angle of Arrival Estimation

A plethora of AOA estimation algorithms exists as outlined in [14]. In [15], angle estimation is done using the space-alternating generalized expectation (SAGE) algorithm for the millimeter wave band centered at 60 GHz, where they used a virtual URA, resulting in poor estimation of the elevation angle.

Frequency invariant beamforming algorithms are used for a UCA in [16], which have the advantage that the beam pattern does not vary over a wide bandwidth rendering themselves useful for UWB applications.

It was demonstrated in [17] the use of the Dolph-Chebyshev weighting for the ULA, URA and UCuA that resulted in all sidelobes being at the same level and the recovery of weaker paths was shown to be possible in contrast to applying uniform weighting methods.

The angle information is obtained using classical beamforming, since it is robust and for the sake of simplicity. This method suffers from lower resolution compared to algorithms like multiple signal classification (MUSIC). Massive sampling in space alleviates the problem of poor resolution of the classical beamforming algorithm.

1.5 Indoor Propagation

In wireless communication systems it is desirable to have line of sight communication for optimal performance. However, this is not always possible especially in indoor environments where the LOS could be blocked by furniture or people. Besides the LOS component the electromagnetic waves and in particular millimeter waves may reach the receiver through three different propagation mechanisms:

- Specular reflection.
- Diffuse scattering.
- Diffraction.

These propagation mechanisms are caused by the nature and material composition of the indoor environment. For example the permittivity (ϵ) and conductivity (σ) of a material determines its ability to reflect or absorb electromagnetic waves. Moreover the material roughness or smoothness determines its interaction with the electromagnetic waves. Smooth surfaces are likely to result in specular reflection while rough surfaces cause diffuse scattering.

In the millimeter wave band the major propagation mechanism of the MPC is specular reflection as shown in [18] with measurement at the center frequency 60 GHz and [4] with measurement at the center frequency 29 GHz.

The latter further compares the different propagation mechanism in 3 different bands. In the millimeter wave band 28 - 30 GHz, the author concludes that it is dominated by specular reflection while in the lower bands, diffuse scattering is quite significant.

In this thesis we investigate the propagation mechanism under the LOS and OLOS conditions.

1.6 Time Dispersion

The time dispersion of the MPC is of great importance in radio planning for millimeter waves. The RMS delay spread σ_τ is used to characterize the time dispersivity of the radio channel [19], [2]. In digital communications, it is a critical parameter for predicting the severity of inter symbol interference (ISI), and consequently the performance of the system. For example in orthogonal frequency division

multiplexing (OFDM), system designers need to choose a guard interval between symbol transmission. The RMS delay spread becomes an important factor in determining how long the guard interval should be.

The coherence bandwidth is the band of frequencies where our signals are highly correlated [18]. It is inversely proportional to the RMS delay spread and it is given as:

$$BW_c = \frac{1}{\sigma_\tau} \tag{1.2}$$

CHANNEL SOUNDING AND MEASUREMENT SETUP

The measurement campaign is carried out using a VNA, Agilent PNA N5772A with a frequency range of 10 MHz to 67 GHz. The Tx antenna is a modified wideband biconical antenna [20],[21], vertically polarized, with a frequency range of 1.5 GHz to 41 GHz and two commercial biconical Rx antennas [22], A-INFOMW P/N:SZ-2003000/P, with a frequency range of 2 GHz to 30 GHz and vertically polarized. The Tx and Rx antennas have an omnidirectional radiation pattern in the azimuth. This ensures that the antenna pattern is not engrained in our results [4].

The Rx antennas are placed at two different locations to measure the LOS and the OLOS simultaneously.

2.1 Measurement Setup

The Tx antenna is connected to port 1 of the VNA, through a flex coaxial cable, A-INFO P/N:2.4M-2.4M-YNL50-1000, of length 50 cm.

The first Rx antenna, Rx2[S21], for the OLOS scenario is connected to port 2 of the VNA, via a 10 m coaxial cable and the channel frequency response is obtained from $S_{21}(f)$.

The second Rx antenna, Rx1[S31], is used for the LOS scenario and it is connected to port 3 of the VNA, through a 5 m coaxial cable. The channel frequency response of the LOS is obtained from $S_{31}(f)$.

The channel remains static throughout the measurement time. The recorded single-input single-output (SISO) frequency responses are then combined in post processing to get a single-input multiple-output (SIMO).

A normalization and calibration procedure was carried out before each measurement campaign, where the Tx and Rx cables were connected back to back and using the VNA inherent normalization setting, the cables were normalized to 0 dB.

The millimeter wave band covered is from 26 - 30 GHz with 1500 frequency points.

2.1.1 VNA setting

The dynamic range in the measurement set up is very critical due to the path loss and loss in the cables particularly to the Rx antennas. Therefore, we need a high dynamic range if we are to resolve highly attenuated paths [23].

One method to increase the dynamic range is to use a small IF bandwidth. However, this comes at a cost of increased measurement time. Table 2.1 outlines the measurement time for the VNA for a bandwidth of 4 GHz and 1500 frequency points, for the different IF bandwidths.

Table 2.1: IF bandwidth setting of the VNA and the corresponding sweep time.

IF Bandwidth [kHz]	Sweep time t_v [s]
0.5	2.8956
1	1.5670
2	0.913
5	0.5107

2.1.2 Parameters

The delay resolution DR and the spatial resolution SR can be calculated as [5]:

$$DR = \frac{1}{BW} \quad (2.1)$$

$$SR = \frac{c}{BW} \quad (2.2)$$

the delay range t on the other hand;

$$t = \frac{N-1}{BW} \quad (2.3)$$

Where BW is the bandwidth, which is 4 GHz, c is the speed of light and N is the number of frequency points, which in this case is 1500.

From this calculation the delay range is 374 ns, the time resolution is 0.25 ns and the spatial resolution is 7.5 cm. The time resolution is quite good as it implies that we are able to distinguish MPC with a delay difference greater or equal to 0.25 ns and the spatial resolution gives us the ability to distinctly identify MPC with a path difference of at least 7.5 cm. This is very important for millimeter wave propagation especially in typical indoor scenarios where many scatterers exists and the wavelength is small compared to the objects commonly found in such scenarios. A delay range of 374 ns, means that we can resolve MPC with as far as 112 m, which is much greater than the dimensions of our room. Moreover, millimeter waves systems are envisaged to work in piconets [1], where the cell radius will be a couple of meters.

In this measurement campaign, an IF bandwidth of 0.5 kHz is used which gives a dynamic range of about 50 dB. Table 2.2 gives a summary of the important parameters for the measurement.

Using the results in table 2.1, for each measurement, the time τ taken to record one channel impulse response (CIR) is approximately:

$$\tau = t_v + t_p = 2.8956 s + 7.5907 s = 10.4864 s \quad (2.4)$$

Table 2.2: Summary of various parameters

Parameter	Value
Transmit Power	11 dBm
Center Frequency	28 GHz
Bandwidth	4 GHz
Trigger out duration	100 ms or 500 ms
IF Bandwidth	500 Hz
C-844 digital input	Channel 0 [pin 14]
C-844 digital output	Channel 6 [pin 24]

where t_v is the VNA sweep time, t_p is the time to move the positioner one step of 0.5 mm.

For the inter-element spacing of 0.4λ which corresponds to 0.4 mm for 30 GHz, $t_p = 6.3838$ s

2.1.3 Antenna Positioner

In this measurement campaign the Physik Instrumente (PI) linear stages positioner is used. The origin repeatability is $1\mu\text{m}$. The origin is set at the "positive limit" for all the axes, hence the downward movement of the Z axis. The unidirectional and bi-directional repeatability are $0.2\mu\text{m}$ and $2\mu\text{m}$ respectively [24].

The antenna positioner is made up of two major components:

- Positioner: PI M-415.DGX [24].
- Precision Motor Controller: C-844 [25].

The PI M-415.DGX is made up of three axes:

- Axis 1: 150 mm.
- Axis 2: 150 mm.
- Axis 3: 50 mm.

Axis 1, 2 and 3 correspond to the X, Y and Z axis respectively in our cartesian coordinates, as indicated in fig 2.1.

2.2 Virtual Antenna Array

The virtual antenna array was made by moving the Tx antenna over predefined positions on the cartesian coordinate. Using the linear positioning stages we can construct three types of virtual arrays.

- ULA.
- URA.
- UCuA.

Our objective in this measurement campaign is to create a virtual UCuA. From the UCuA, we can easily extract a ULA and a URA. The UCuA can be viewed as several layers of a URA, shown in fig. 2.2.

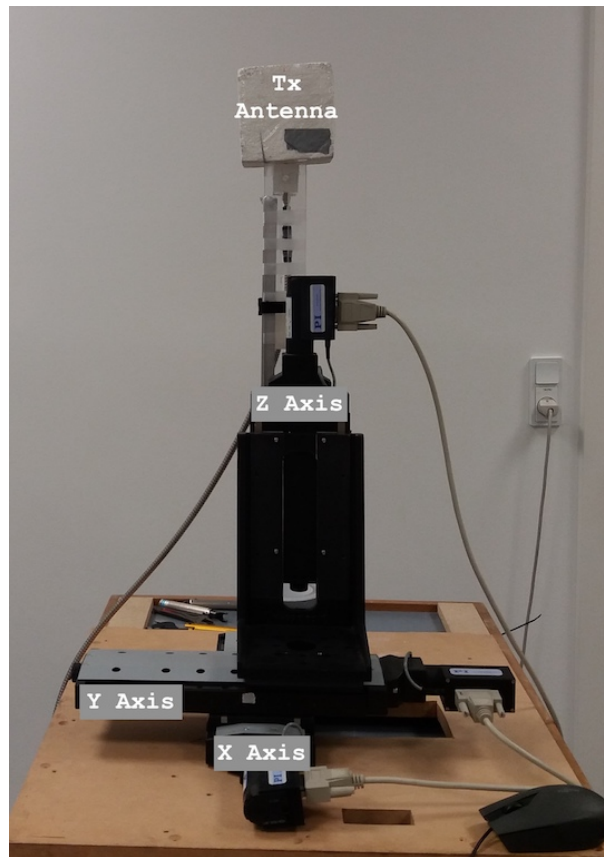


Fig. 2.1: Positioner Cartesian Coordinates Mapping.

The virtual UCuA has an aperture of 12λ by 12λ by 4λ with an inter-element spacing of 0.4λ and 15λ by 15λ by 5λ with an inter-element spacing of 0.5λ where λ is for 30 GHz.

Fig. 2.2 shows the geometry of the virtual URA. The antenna positions are determined by the algorithm that was developed for controlling the positioner, whose objective was to reduce the measurement time.

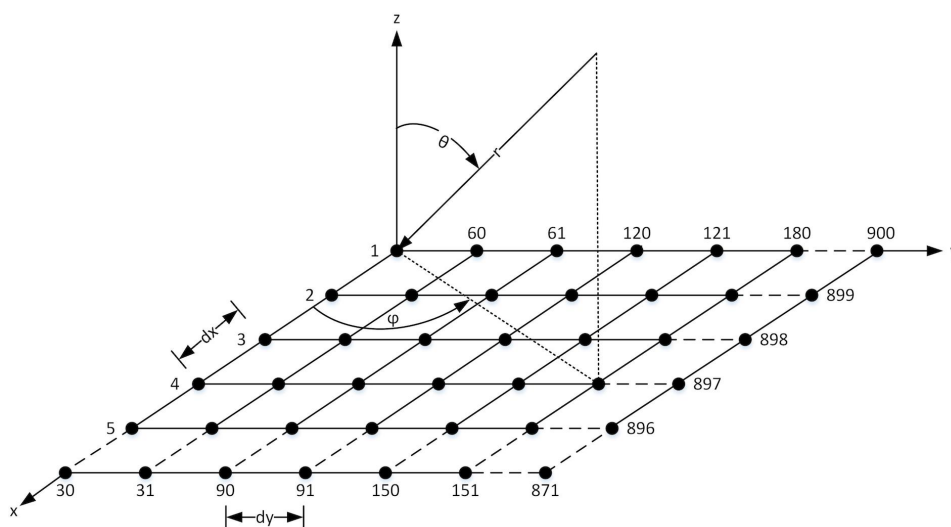


Fig. 2.2: Virtual URA geometry.

Fig. 2.3 illustrates the cuboid. The azimuth angle φ is in the range $0^\circ - 360^\circ$, while the elevation angle, θ is in the range $0^\circ - 180^\circ$.

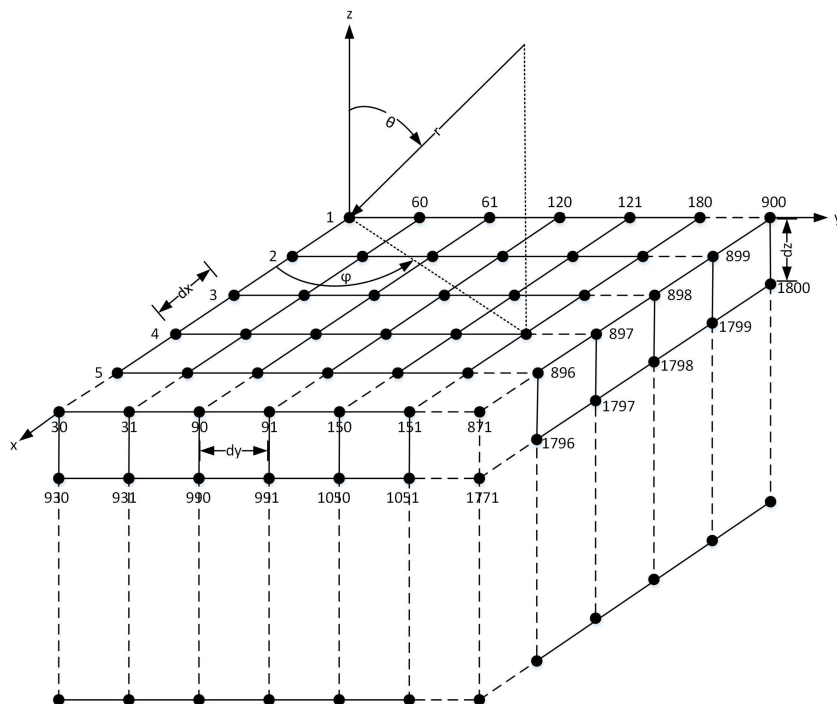


Fig. 2.3: Virtual UCuA geometry.

2.3 Measurement Procedure

In the measurement campaign, the channel was sampled massively in space. To achieve this goal an automatic control system had to be built. The objective was to synchronize the VNA and the antenna positioning system. The automation software was built with Python so as to be platform independent, therefore a Windows, Mac OS or Linux personal computer (PC) can be used. The PyVisa instrument control library [26] was used in order to communicate to the C-844 motor controller via standard commands for programmable instruments (SCPI) commands. The VNA has a custom program saves the data on its internal hard disk while the Python script records a log file on the PC for all the antenna positions. Communication to the C-844 motor controller is via RS232, where a USB-to-serial converter was used.

2.3.1 Automation of Antenna Positioning System

The control software supplied along with the C-844 only supported movement to a particular position, one point at a time, requiring the user to input the desired positions manually. Recording massive amounts of channel frequency responses, can be a daunting task, both physically and accuracy of the results would not be guaranteed as it would mean keeping the environment static for several days and the need for constant recalibration of the system. The Python script created reduced the measurement time to about 25 hours.

The measurement is done in phases, i.e, the UCuA is divided into two or three parts. This is because the C-844 motor controller becomes unresponsive on average after 12 hours of continuous operation.

An external fan was added for the C-844 motor controller and it was raised about 10 cm above the floor to avoid over heating, nonetheless after about 16 hours of continuous operation the C-844 motor controller became unresponsive.

Measurement in phases solved this problem, after the first phase the C-844 motor controller is switched

off for a while before beginning the next phase.

2.3.2 Flow control

The automated measurement process is illustrated in fig. 2.4. The positioner moves along the X-axis and on reaching the last point of the X-axis it changes to the next Y-position. The positioner then reverses along the X axis from the last point towards zero to save time during measurement and avoid a barren cycle.

This is repeated until all points on the XY plane are covered. The positioner then moves the Z-axis to the next position, and moves the X and Y axes to zero and the process is repeated.

The process can be summarized as follows:

1. The python script creates an object for establishing communication with the C-844 precision motor controller.
2. The python script initializes the C-844 controller by setting the important parameters of acceleration and velocity.
3. The positioner is set to the reference position.
4. The C-844 is reset and initialized again to take the “HOME” position.
5. The C-844 motor controller sends a transistor transistor logic (TTL) rising edge trigger to the VNA to take measurements.
6. The VNA sends a TTL falling edge trigger to the C-844 when the measurement is done.
7. The PC polls the C-844 to determine if the measurement was done and sends a move command to the C-844 for the next position.
8. The C-844 moves the axes to the position desired and processes 5 to 7 are repeated.

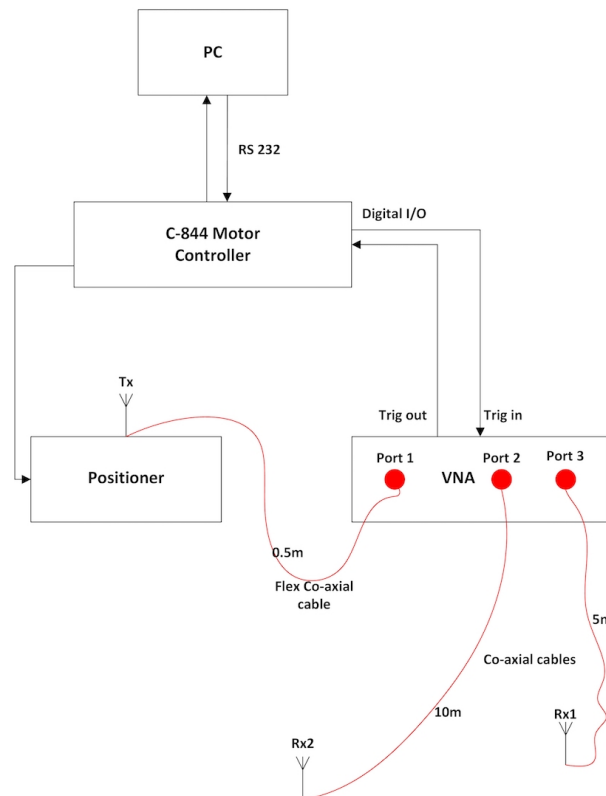


Fig. 2.4: Measurement Setup: RF cables are in red.

2.3.3 Phase Test

Prior to the measurement a phase test was carried out to investigate the phase variation due to the cable movement of the flex coaxial cable. This was done by measuring $S_{11}(f)$ as the antenna was moved to the eight vertices of the cuboid, 150 mm by 150 mm by 50 mm. The phase variation in the frequency range 26 - 30 GHz was then recorded at each vertex. The cable was calibrated to 0 dB before measurement, and as shown in fig.2.5b and fig.2.5a, the magnitude variation was by a maximum of 0.1 dB on all the vertices for all the frequency range and the phase variation was a maximum of 2.5° .

The subscripts N and P in fig. 2.5 represent the negative and positive limits respectively of the axes.

2.4 Measurement Scenario

The measurements were carried out in Aalborg University APNet section kitchen; room 1.202, SELMA LAGERLØFS VEJ 312, Aalborg 9220, Denmark. The room geometry is as shown in fig. 2.6. The room is located on the second floor of a three storey building.

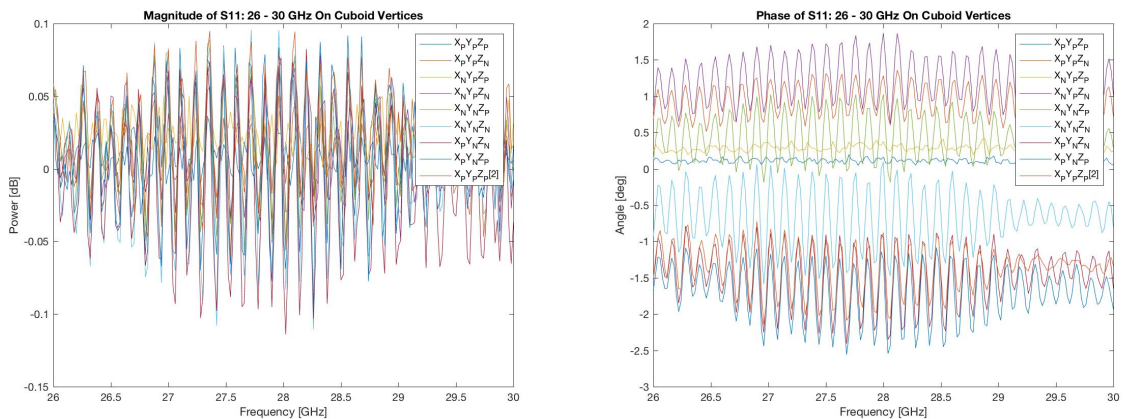
The wall next to the door and the wall next to the fridge are made of plasterboard whereas the walls where the windows are located are made of concrete. The floor is made of concrete.

The windows are double glazed glass with metallic locks and frames. The window area has a cavity of 45 cm with a 1.5 cm layer of wood. Along the windows there is a cable trunk for the electric cables in the room, made on the top part by wood and the sides are made of plastic.

The room dimensions are 7.36 m by 5.54 m, and the height from the floor to the ceiling is 2.835 m. The ceiling is a dropped ceiling with ceiling tiles. The height from the floor to the concrete ceiling (without the ceiling tile) is 3.534 m. On the dropped ceiling there is a metallic air-conditioning system as shown in fig. 2.10. Inside the 0.7 m cavity, there are the metallic air conditioner pipes though not visible in the photos.

There are metallic radiators raised from the floor by 9.5 cm under each window and having a height of 31.5 cm from the floor.

Next to the wooden table in fig. 2.10, there is a whiteboard whose dimensions are 240 cm by 122 cm with a thickness of 1.5 cm, that spans from one edge of the window to the other edge of the other window.



(a) Magnitude of $S_{11}(f)$.

(b) Phase of $S_{11}(f)$.

Fig. 2.5: Variation of phase and magnitude due to movement of the flex coaxial cable.

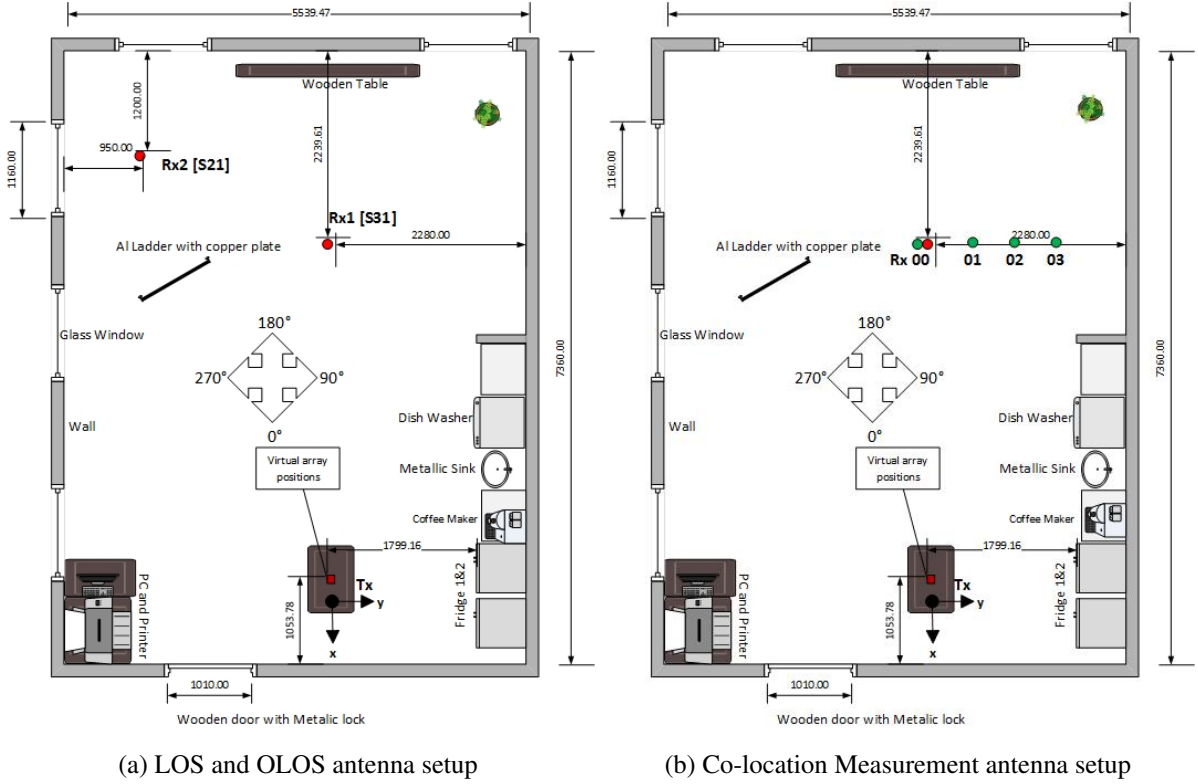


Fig. 2.6: Antenna Location with respect to room geometry: All dimensions in mm.

The antenna heights are as outlined in table 2.3. The antenna heights were selected to give a good clearance above the floor and below the ceiling, while at the same time placing them on the same elevation level.

Table 2.3: Antenna heights in meters: Measurement campaign 1 and 2.

Antenna Height [m]	Tx	Rx1 [S31]	Rx2 [S21]
From Top of Antenna to the Floor	1.499	1.472	1.472
From Top of Antenna to the Ceiling	1.361	1.347	1.342
From Centre of Antenna to the Floor	1.452	1.455	1.456
From Centre of Antenna to the Floor	1.363	1.381	1.381

2.4.1 Measurements Campaigns

The measurement campaigns were carried out on two different occasions:

- Measurement campaign 1: with an inter-element spacing of 0.5λ .
- Measurement campaign 2: with an inter-element spacing of 0.4λ .

2.4. Measurement Scenario

In measurement campaign 1, with an inter-element spacing of 0.5λ , the room did not have the white board in fig. 2.8a installed behind the Rx1[S31] antenna. This had a significant effect on the results as will be shown in chapter 3. The location of furniture in the room was as shown in fig. 2.6 and fig. 2.7. The obstructor was also constructed differently as explained in section 2.4.3. In measurement campaign 2, with an inter-element spacing of 0.4λ , the room had a coffee machine installed whereas two wooden tables and a wooden cup-board had been removed.

The measurements carried out were:

1. LOS for the UCuA which was recorded in the VNA as $S_{31}(f)$ with antenna Rx1[S31].
2. OLOS for the UCuA which was recorded in the VNA as $S_{21}(f)$ with antenna Rx2[S21].
3. Measurement with antennas co-located as shown in fig. 2.6b and fig. 2.7b.

In the first and second measurement setup, the measurement was done simultaneously for the virtual UCuA.

2.4.2 Co-Location Measurement

The third measurement with the antenna co-located is as shown in fig. 2.6b and fig. 2.10.

The antenna Rx1[S31] is kept at the original position as in the first two measurements then the Rx2[S21] antenna, shown by the green dot in fig. 2.6b, is placed in four different locations each separated by 0.5 m.

It is worth to note that the environment was kept as in fig. 2.7a with the only change being the location of antenna Rx2[S21]. This measurement was carried out for the YZ plane thus, 300 CIR were recorded for each of the four different locations, for each of the two Rx antennas.

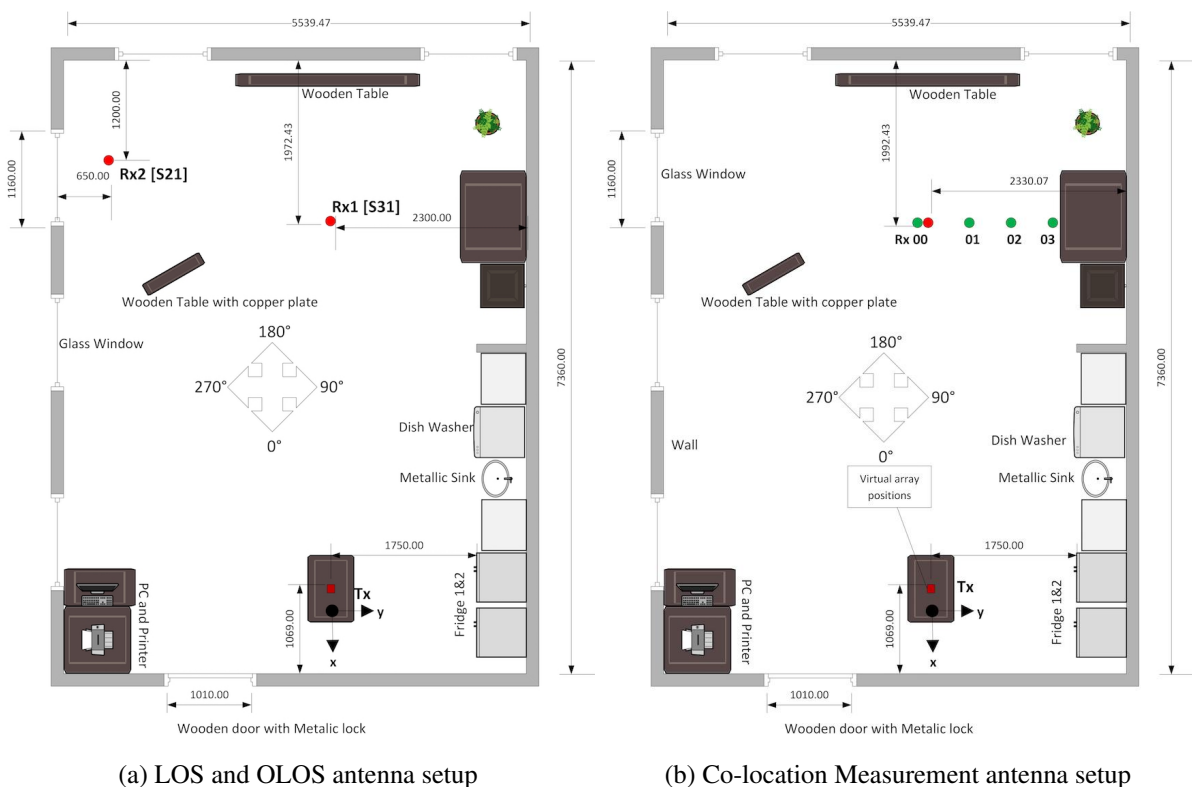


Fig. 2.7: Antenna Location with respect to room geometry, campaign 1: All dimensions in mm.

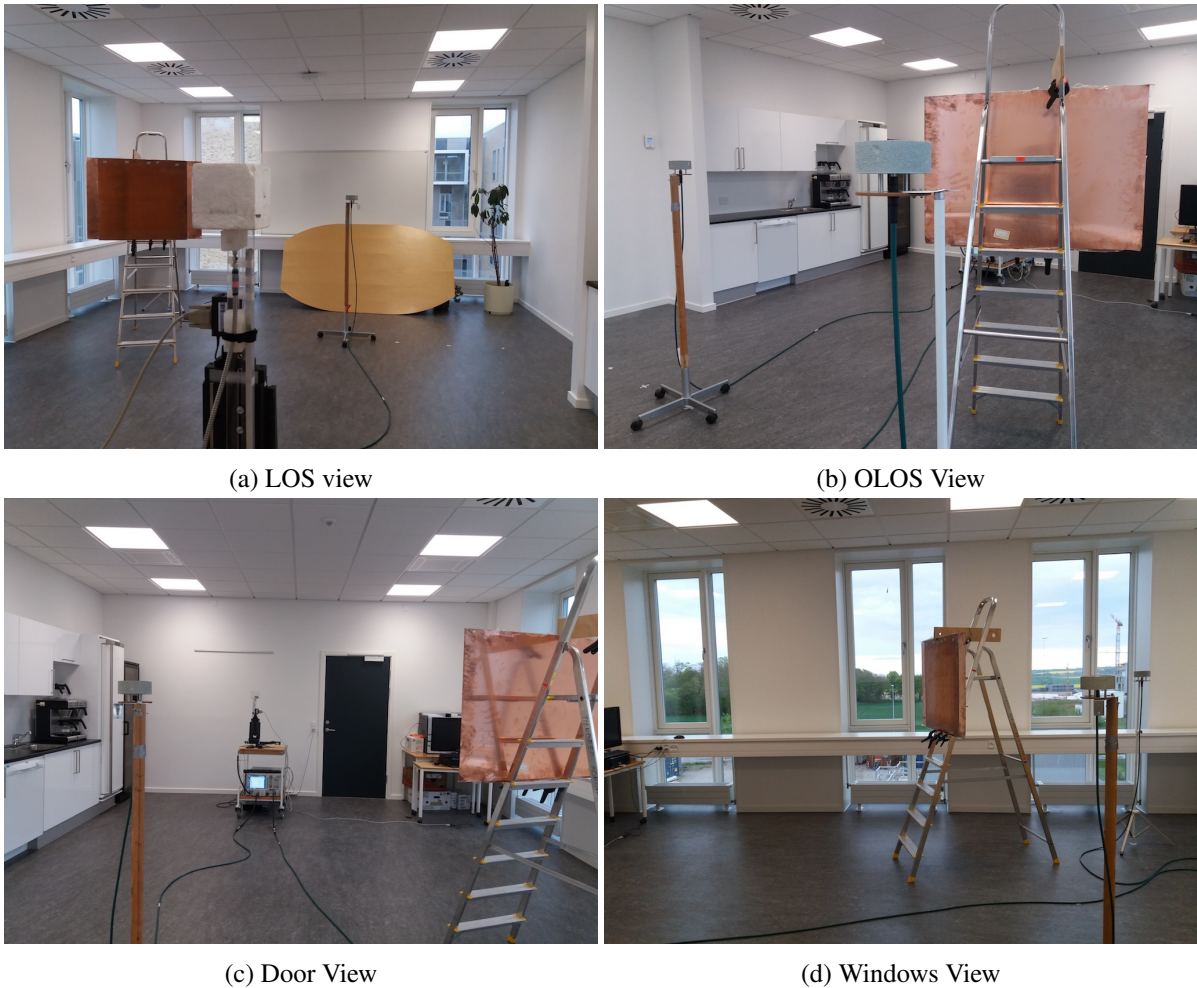


Fig. 2.8: Room Photos: Measurement campaign 2 (LOS and OLOS).



Fig. 2.9: Panorama view of the kitchen: Measurement campaign 1.

2.4.3 Obstructor

To create the OLOS scenario an obstructor was placed between the Rx2[S21] antenna and the Tx antenna as shown in fig. 2.8. The separation distances are given in table 2.4.

The obstructor was made by attaching a copper plate onto an aluminium ladder. The copper plate dimensions are: Length: 1 m Height: 0.74 m.

Obstructor for measurement campaign 1, with spacing Inter-element 0.5λ

The obstructor was made of a wooden table placed up right with a copper plate attached to the top part of the table. Table Dimensions: Length: 0.78 m Height: 1.550 m

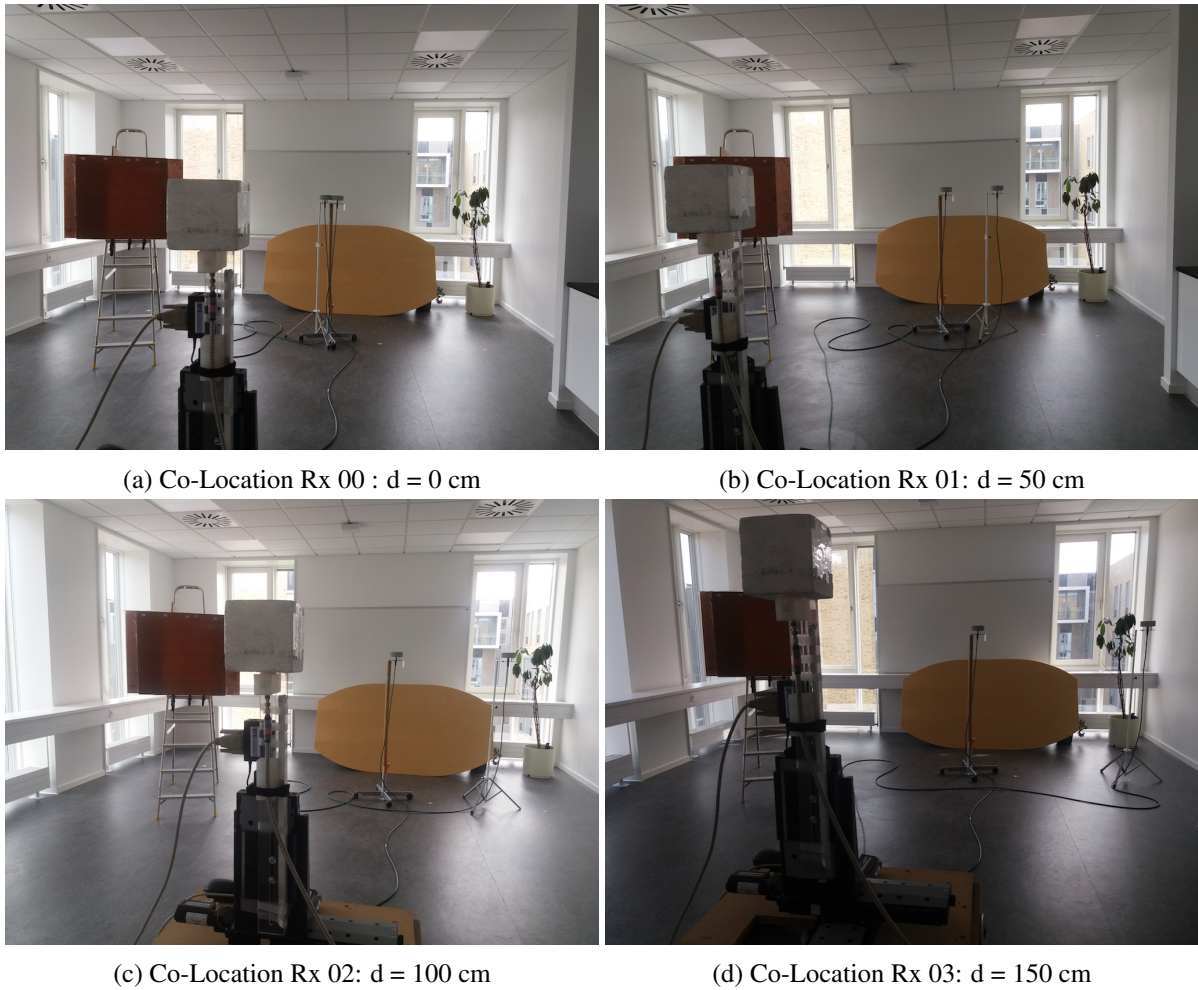


Fig. 2.10: Room Photos: Co-Location Measurement (campaign 2), where d is the separation distance of the two antennas.

Table 2.4: Obstructor distance for measurement campaign 2, with an inter-element spacing of 0.4λ .

Description	Distance [m]
Tx antenna to Obstructor	3.905
Rx2[S21] antenna to Obstructor	1.703
Obstructor to floor	1.036
Obstructor to ceiling	1.041

Table 2.5: Obstructor distance for measurement campaign 1, with an inter-element spacing of 0.5λ .

Description	Distance [m]
Tx antenna to Obstructor	4.129
Rx2[S21] antenna to Obstructor	1.341
Obstructor top to floor	1.550
Obstructor to ceiling	1.295
Height above floor of Copper Plate	0.809

RESULTS AND ANALYSIS

3.1 The Indoor Propagation Channel

Consider a UCuA composed of L elements along the x-axis, M elements along the y-axis, N elements along the z-axis, with the inter-element distance $d_x = d_y = d_z = d$. The inter-element distance is chosen to be $d = 0.4\lambda$ to avoid spatial aliasing.

The origin of the coordinate system as shown in fig 2.2 is taken as the time reference [27].

Now suppose that the CIR between the Tx and origin of the UCuA is made up of K multipath waves [4]. The wave front impinging on the virtual antenna array is well approximated by a plane wave since the virtual antenna array is in the far field region.

The far field assumption holds true when the $d_r \gg \lambda$ and $d_r \gg D$

$$d_r = \frac{D^2}{\lambda} \quad (3.1)$$

where D is the antenna aperture, d_r is the distance between the Tx and Rx antennas, and λ is the wavelength.

The channel frequency response $H(f)$ is obtained as:

$$H(f) = \sum_{k=0}^{K-1} \alpha_k e^{-j2\pi f \tau_k} \quad (3.2)$$

τ_k is the delay of the k-th path with complex amplitude α_k .

The time taken, by the k-th plane wave impinging on the array with an AOA, (θ_k, φ_k) to reach the element l, m, n , with respect to the reference element at the origin of the coordinate system $(0, 0, 0)$, is given as:

$$\tau_{kl,m,n}(\theta_k, \varphi_k) = \frac{r_{l,m,n} \cdot \hat{y}(\theta_k, \varphi_k)}{c} \quad (3.3)$$

where:

$\underline{r}_{l,m,n}$ - the position vector of the element l, m, n which is defined as;

$$\underline{r}_{l,m,n} = \begin{pmatrix} d_x(l-1) \\ d_y(m-1) \\ d_z(n-1) \end{pmatrix} \quad (3.4)$$

$\hat{\underline{v}}(\theta_k, \varphi_k)$ - the unit vector in the direction (θ_k, φ_k) which is defined as;

$$\hat{\underline{v}}(\theta_k, \varphi_k) = \begin{pmatrix} \sin\theta_k \cos\varphi_k \\ \sin\theta_k \sin\varphi_k \\ \cos\theta_k \end{pmatrix} \quad (3.5)$$

(\cdot) - the dot product.

c - the speed of light.

The frequency response $H_{l,m,n}(f)$ of the l, m, n -th element is given as:

$$H_{l,m,n}(f) = \sum_{k=0}^{K-1} \alpha_k e^{-j2\pi f(\tau_k + \tau_{k,l,m,n})} \quad (3.6)$$

The element frequency response $H_{l,m,n}(f)$ is thus seen to be a phase shifted version of $H(f)$ [4].

The array frequency response $H(f, \theta, \varphi)$, is obtained by summing the frequency response of each element, $H_{l,m,n}(f)$ multiplied by a complex weight $w_{l,m,n}$ to shift its responses into alignment with the reference element which is at the origin of the coordinate system, hence:

$$H(f, \theta, \varphi) = \frac{1}{N} \frac{1}{M} \frac{1}{L} \sum_{n=0}^{N-1} \sum_{m=0}^{M-1} \sum_{l=0}^{L-1} w_{l,m,n} H_{l,m,n}(f) \quad (3.7)$$

The weighing vector $w_{l,m,n}$ is given as:

$$w_{l,m,n} = e^{-\frac{j2\pi}{\lambda} \underline{r}_{l,m,n} \cdot \hat{\underline{v}}(\theta_k, \varphi_k)} \quad (3.8)$$

The angle information is obtained via classical beamforming. Classical beamforming works by shifting the elements frequency response back to the reference position. A steering vector is generated for each search angle (θ_0, φ_0) . The maximum power is obtained when the search angle (θ_0, φ_0) is equal to the AOA (θ_k, φ_k) of the K -th wave.

By taking the inverse discrete fourier transform (IDFT) (performed using the inverse fast fourier transform (IFFT) algorithm) of the array frequency response $H(f, \theta, \varphi)$, we can obtain the spatial-temporal CIR, $h(t, \theta, \varphi)$ as:

$$h(t, \theta, \varphi) = \sum_{n=0}^{N-1} H(f_n, \theta, \varphi) e^{j2\pi f_n t} \quad (3.9)$$

where f_n is the n-th frequency bin.

3.2 Power Delay Profile

From the frequency response of the l, m, n -th element $H_{l,m,n}(f)$, eq. 3.6, we can obtain the temporal response of the channel $h(t)$ by performing the IDFT of $H_{l,m,n}(f)$. Thus $h(t)$ is given as:

$$h(t) = \sum_{n=0}^{N-1} H_{l,m,n}(f) e^{j2\pi f_n t} \quad (3.10)$$

The PDP $P(t)$ shows how the power of the transmitted signal is distributed in time and it is the absolute square of the channel temporal response, defined as [6]:

$$P(t) = |h(t)|^2 = \sum_{k=0}^{K-1} \alpha_k^2 \delta(t - \tau_k) \quad (3.11)$$

where $\delta(\cdot)$ is the dirac delta function, τ_k is the delay of the k-th path and α_k the complex amplitude.

The average power delay profile is obtained by taking an average of each element CIR in the UCuA in order to remove the effects of fast fading [5].

Fig. 3.1 compares the CIR along the element positions of the UCuA for the two measurement campaigns. In the LOS scenario the dynamic range is chosen as 35 dB from the highest peak whereas in the OLOS scenario, a 30 dB dynamic range is chosen. Moreover the time axis is limited to 85 ns for the LOS scenario and 75 ns for the OLOS scenario, since beyond these time limits no significant paths are observable.

The effect of furniture change is more pronounced on the tail of the average PDP as can be seen in fig. 3.2. The average PDP is carried out over 8100 CIR in fig. 3.1a and fig. 3.1b. In fig. 3.2c and fig. 3.2d, the average PDP is considered for the co-location Rx 00 and Rx 03 shown in fig. 2.6b. In this case the average PDP consists of 300 CIR. At location Rx 00 the reflectivity of the whiteboard causes multiple reflections which are less compared to location Rx 03.

3.3 Fresnel Zone

In LOS communication, objects located within the Fresnel zones could cause signals to be diffracted and arrive at the receiver out of phase or in phase with the LOS component. The first three Fresnel zones are the most significant. When the signals arrive at the receiver out of phase they could result in destructive interference, whereas when they arrive in phase they result in constructive interference.

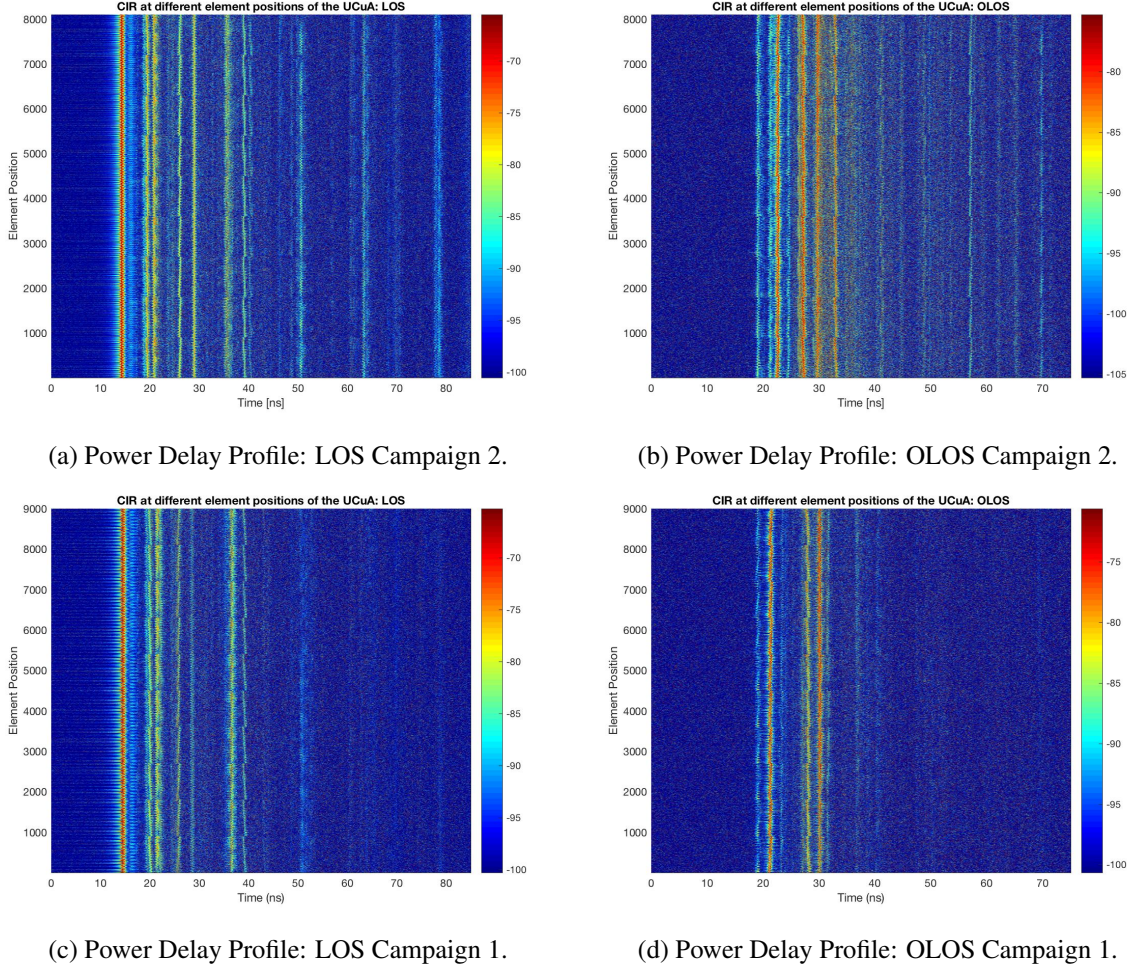


Fig. 3.1: A comparison of the PDP for the two measurement campaigns

When constructing the obstructor to create the OLOS, the objective was to have at least the first three Fresnel zones blocked.

The radius of the n^{th} fresnel zone is calculated as:

$$F_n = \sqrt{\frac{n\lambda d_1 d_2}{d_1 + d_2}} \quad (3.12)$$

From table 2.4 and 2.3, the difference in height between the antenna and the top most part of the obstructor was 0.348m whereas the height difference with the bottom most part of the obstructor was 0.416m. From eq. 3.12, the first 3 fresnel radii for 30 GHz are 0.1089m, 0.1539m and 0.1885m respectively. This implies that the obstructor completely covered the first three fresnel zones as will be shown in section 3.4.

3.4 Power Angle Delay Profile

The PADP indicates that the most significant MPC for the LOS are due to specular reflection. This coincides with the results in [4], where the analysis was carried on the millimeter wave band 28 - 30 GHz using a virtual UCA.

3.4. Power Angle Delay Profile

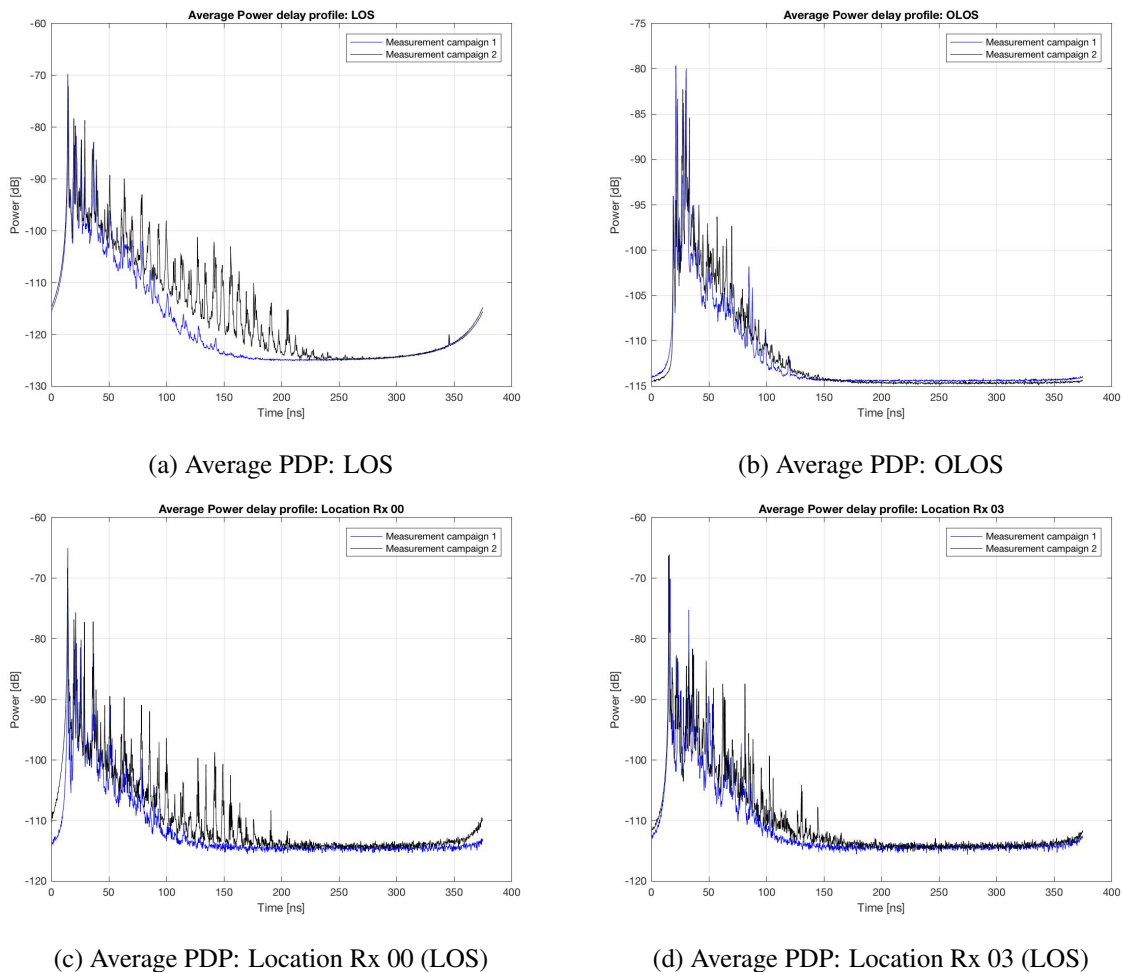


Fig. 3.2: A comparison of the average PDP for the two measurement campaigns.

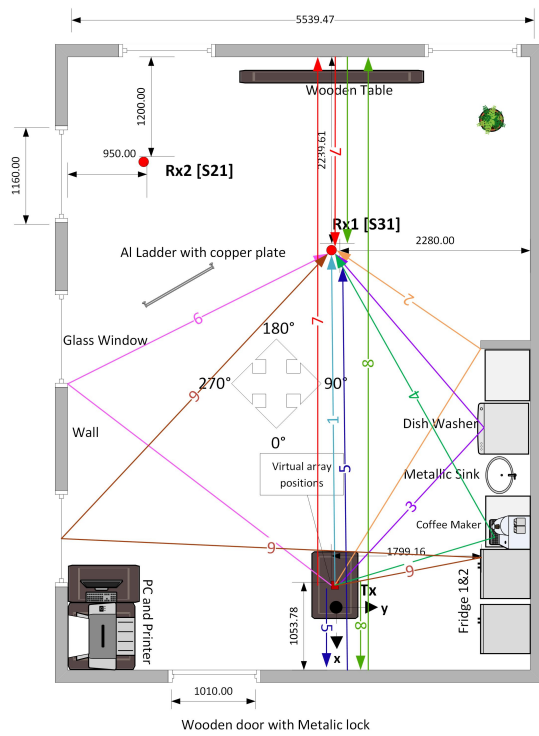
The back and forth reflections due to the walls in the LOS scenario can be seen in paths 5, 7 and 8 in fig. 3.3a and in fig. 3.4a for measurement campaign 2 and in fig.3.3c and fig. 3.4c for measurement campaign 1. Path 2 and 6 are interesting to note in that the structure of the room greatly influences the propagation mechanism. Path 2 is due to a wedge-like corner of the plaster board protruding in the room. On the other hand the wedge-like structure of the window described in section 2.4, is seen to contribute to path 6 as shown in fig. 3.3a and in fig. 3.4a.

Path 9 is due to multiple bounce specular reflection by the metallic handle of the white fridge shown in fig. 2.8c and the window as shown in fig. 3.3a.

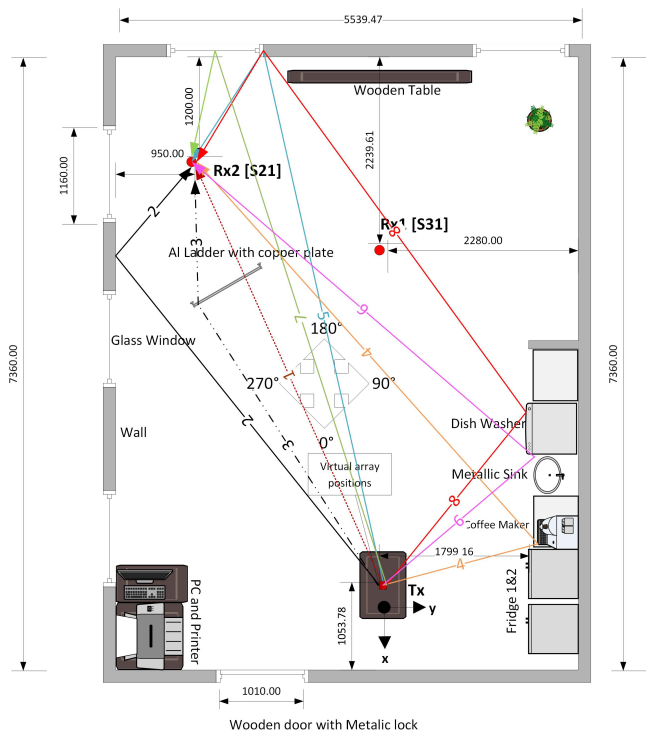
In the OLOS, diffuse scattering is a significant propagation mechanism. As shown in fig. 3.4b, paths from diffuse scattering outnumber those from specular reflection albeit with lower power.

It can be seen that diffraction is a significant propagation mechanism in the OLOS scenario. Path 1 and 3 in fig. 3.3b and fig. 3.4b are most likely due to diffraction by the aluminum ladder, owing to the fact that the radii of the first 3 fresnel zones were completely covered by the copper plate. Diffraction is also observed for the OLOS in [15].

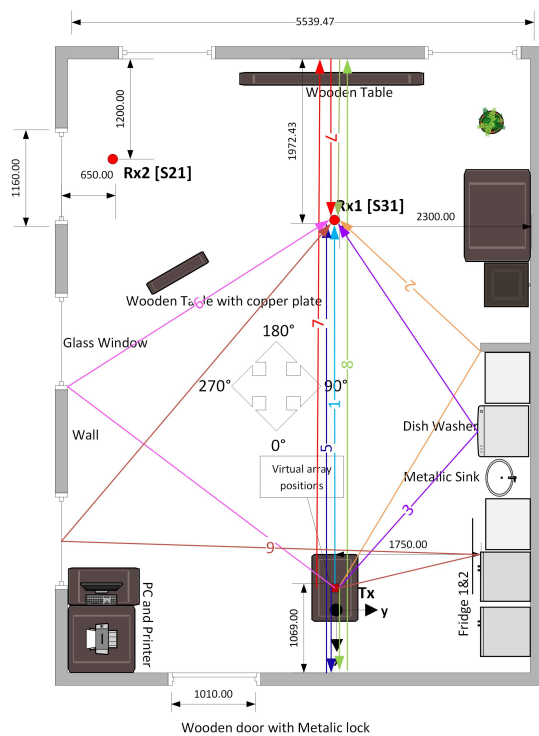
Although specular components dominate in millimeter wave communication, diffraction from edges should be considered keenly when designing channel models for 5G. In these results the path 2 and 6 for the LOS are most likely due to edge diffraction. In [28] extensive measurements are carried out to investigate the effect of this phenomena in millimeter waves.



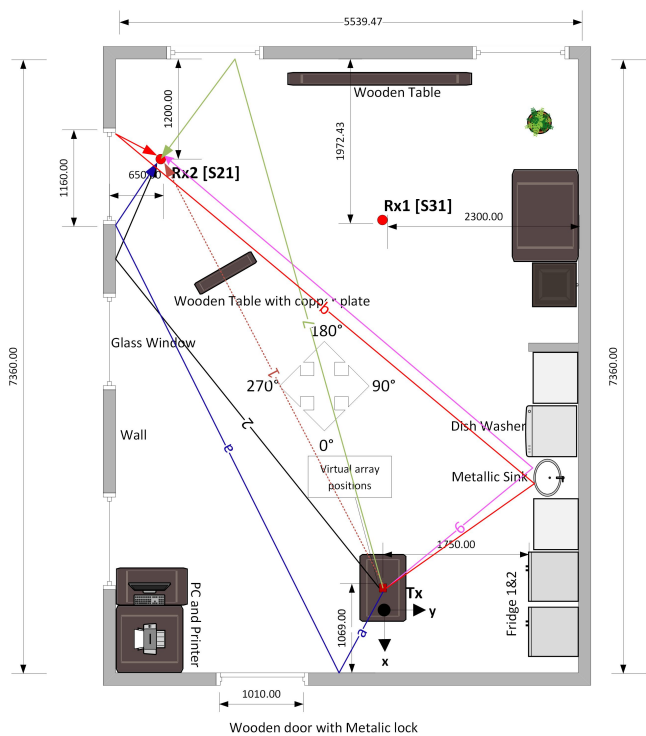
(a) Paths identified for LOS: campaign 2



(b) Paths identified for OLOS: campaign 2



(c) Paths identified for LOS: campaign 1



(d) Paths identified for OLOS: campaign 1

Fig. 3.3: Propagation paths in relation to room geometry: All dimensions in mm.

3.4. Power Angle Delay Profile

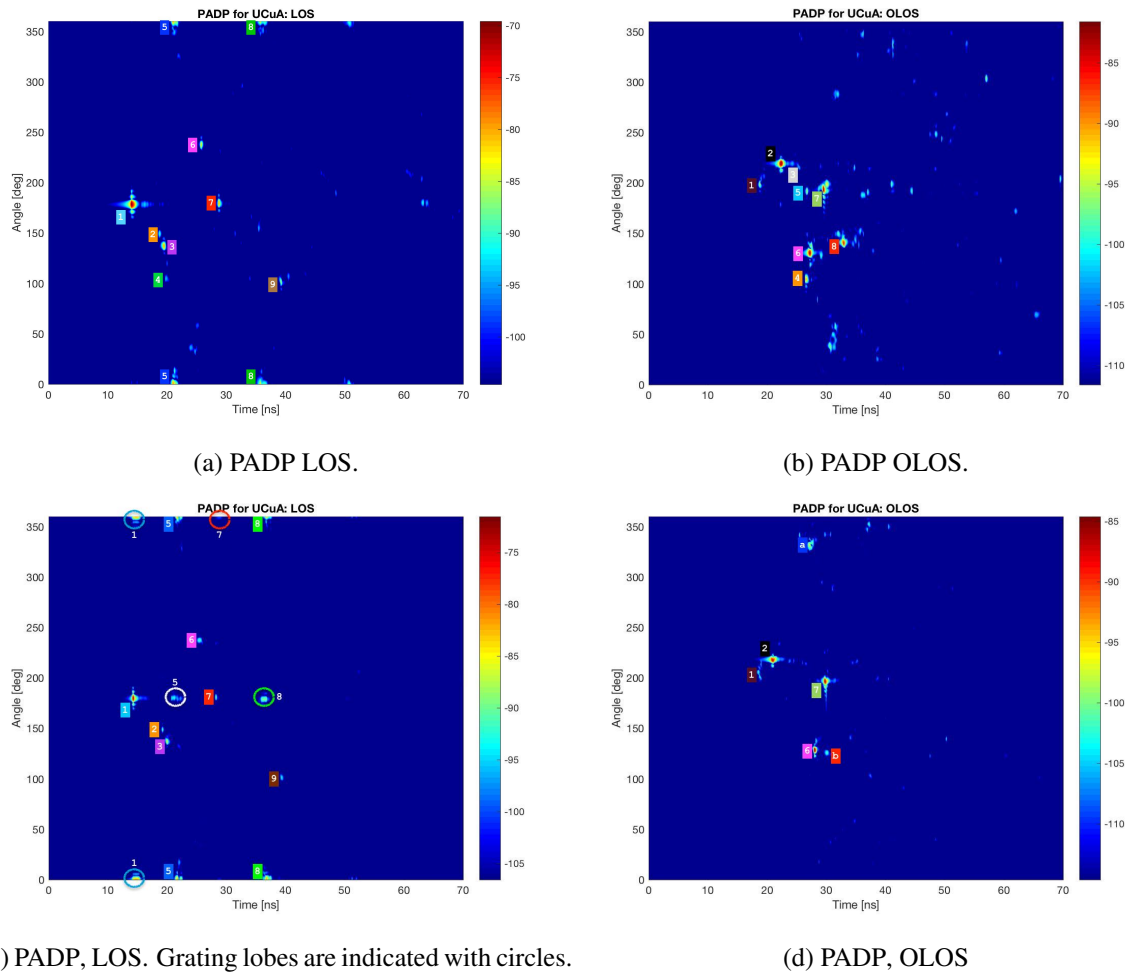


Fig. 3.4: PADP for measurement campaign 1 [3.4c,3.4d] and measurement campaign 2 [3.4a,3.4b].

Table 3.1 and 3.2 outline the identified propagation paths and the power levels in dB for the LOS and OLOS scenarios respectively for measurement campaign 2. The difference in power between the strongest MPC in the OLOS and the LOS component is 12 dB.

Fig. 3.4 and 3.3 show the identified paths in both measurement campaigns. In fig. 3.3a, path 4 is seen to come from the coffee machine which has metallic front part.

On the other hand for the OLOS, the specular and diffuse paths seem to increase in the second measurement campaign. This is most likely to have been caused by two factors: the change in the wall reflectivity and the type of obstructor used, since the ladder could contribute to edge diffraction whereas the obstructor in the first measurement campaign covered the LOS from the ground level. The whiteboard is most likely to have contributed to path 5 and 8 in the OLOS scenario of measurement campaign 2, since these paths were not present in the first measurement campaign.

In fig. 3.4b, two paths (**a** and **b**) are identified that are not in the second measurement campaign. Path **b** is most likely to have been blocked by the obstructor in the second measurement campaign due to a slight change in the location of the obstructor.

In both the LOS and OLOS scenarios, it is interesting to see the similarities in the paths detected. Having conducted the measurement 3 weeks apart the similarities show the robustness of this measurement system as well as its repeatability.

Table 3.1: Propagation paths and the corresponding power levels: LOS, measurement campaign 2.

Path	Angle [deg]	Delay [ns]	Distance [m]	Power [dB]
1	178.5	14.25	4.272	-70.03
2	149.4	18.75	5.621	-89.88
3	137.4	19.5	5.846	-78.51
4	105.3	19.75	5.921	-86.04
5	0	21	6.296	-80.57
6	236.7	26	7.795	-82.89
7	179.5	29	8.694	-78.76
8	0	-84.7	10.942	-84.7
9	101.3	39.25	11.777	-87.51

Table 3.2: Propagation paths and the corresponding power levels: OLOS, measurement campaign 2.

Path	Angle [deg]	Delay [ns]	Distance [m]	Power [dB]
1	198.6	19	5.696	-95.19
2	218.6	22.75	6.820	-84.52
3	212	25.5	7.645	-100.2
4	103.3	26.5	7.645	-89.9
5	191.5	26.75	8.019	-91.10
6	130.4	27.25	8.169	-82.54
7	192.5	29.75	8.919	-83.65
8	140.4	33	9.89	-86.39

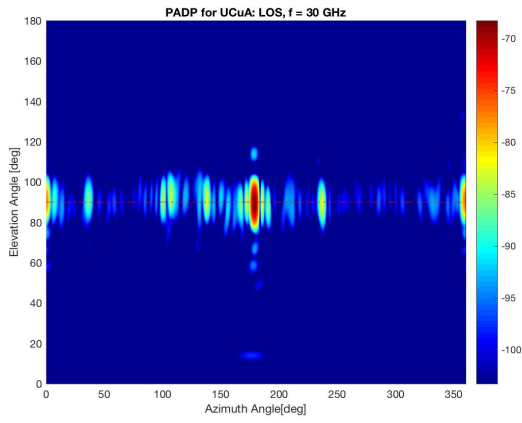
3.4.1 Elevation Angle

A joint azimuth and elevation angle estimation for the UCuA was done for the center frequency 28 GHz, the start frequency 26 GHz and the stop frequency 30 GHz. The results are as shown in fig. 3.5 for the LOS and the OLOS scenario in measurement campaign 2.

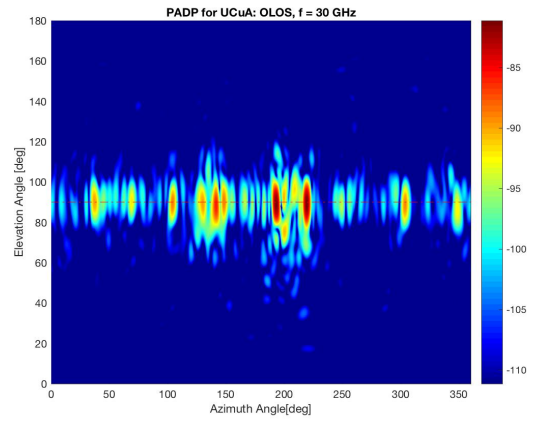
Since the Tx and Rx height were at the same height, it follows that most of the propagation of the dominant path lie along the same plane, 90° . The antenna array pattern acts as a spatial filter in this case. In the E-plane of the two commercial antennas [22], the attenuation varies from as low as -20 dB to -10 dB in the frequency band 26 - 30 GHz.

In the azimuth angle φ estimation for the URA and UCuA, the gains in terms of resolution of the MPC seem minimal however when a joint azimuth and elevation angle θ is done it is clear that a URA does not have a good resolution of the elevation angle [10]. The UCuA, therefore becomes favourable tool when the elevation angle information is required.

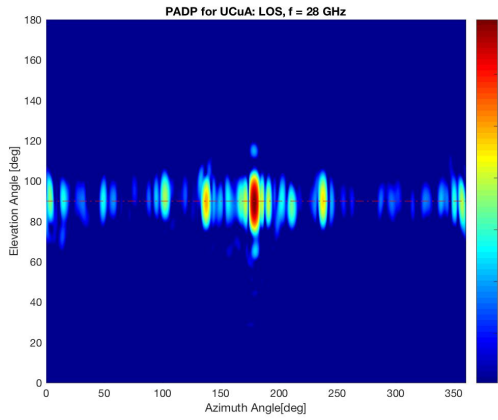
3.4. Power Angle Delay Profile



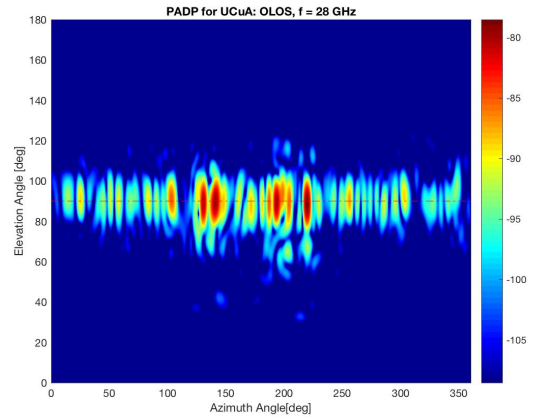
(a) Elevation angle for LOS: 30 GHz



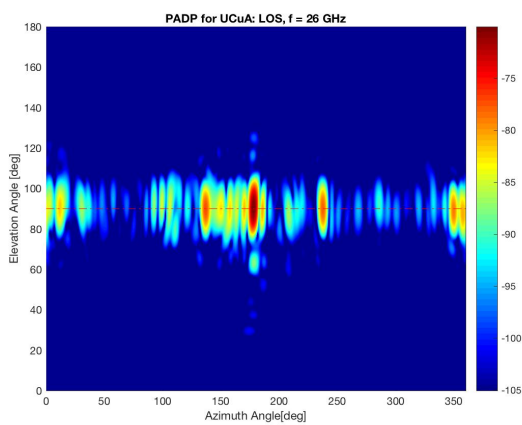
(b) Elevation angle for OLOS: 30 GHz



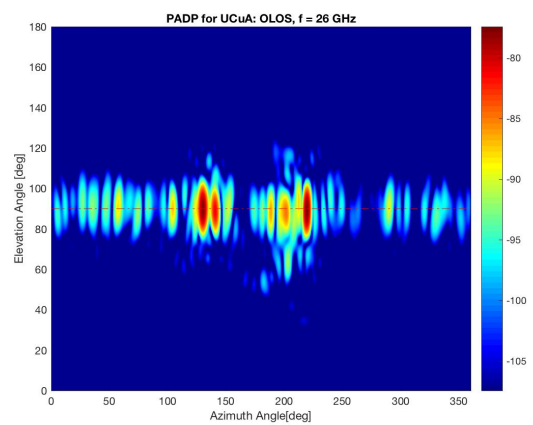
(c) Elevation angle for LOS: 28 GHz



(d) Elevation angle for OLOS: 28 GHz



(e) Elevation angle for LOS: 26 GHz



(f) Elevation angle for OLOS: 26 GHz

Fig. 3.5: Elevation angle for the start, center and stop frequency, measurement campaign 2.

3.5 RMS Delay Spread

The RMS delay spread σ_τ is a measure that characterizes the time dispersion of the signal. It is defined as the square root of the second central moment of the PDP [2]:

$$\sigma_\tau = \sqrt{\overline{\tau^2} - (\overline{\tau})^2} \quad (3.13)$$

where:

$$\overline{\tau^2} = \frac{\sum_k P(\tau_k) \tau_k^2}{\sum_k P(\tau_k)} \quad (3.14)$$

$$\overline{\tau} = \frac{\sum_k P(\tau_k) \tau_k}{\sum_k P(\tau_k)} \quad (3.15)$$

$\overline{\tau}$ is the mean excess delay, which is the first central moment and $\overline{\tau^2}$ is the second central moment of the PDP.

$P(\tau_k)$ is the power in mW of the delay bin corresponding to the delay bin τ_k .

In literature, when calculating the RMS delay spread, a noise floor is defined so as to exclude the noise bins in the calculation. However, the selection of this noise floor is a factor that varies from system to system and largely depends on the dynamic range of the measurement equipment.

In [29], a 50 dB margin is used in the calculation of the RMS delay spread whereas, in [30] a 30 dB margin is used for both the LOS and OLOS scenarios at the center frequency 60 GHz.

The RMS delay spread for both measurement campaigns is as outlined in table 3.3, using a dynamic range of 25 dB for the LOS and OLOS scenarios.

Table 3.3: RMS delay spread (σ_τ) and mean excess delay ($\overline{\tau}$) for different noise floor in the LOS and OLOS scenarios.

Measurement Campaign	LOS		OLOS	
	$\overline{\tau}$ [ns]	σ_τ [ns]	$\overline{\tau}$ [ns]	σ_τ [ns]
1	22.7	8.8	32.6	11.5
2	25.4	13.6	41	16.4

A change of furniture in the room is the most likely cause of the abrupt change in the RMS delay spread. Two wooden tables and a cupboard were removed whereas a whiteboard and a coffee machine were installed in the second measurement campaign. The other notable difference was in the obstructor as outlined in section 2.4.3. The antenna aperture also reduced due to the use of an inter-element spacing of 0.4λ . Among these factors the most likely cause of this increase in the RMS delay spread is the change of the wall reflectivity.

This was also reported in [18], where the RMS delay spread increased with increased reflectivity of the walls, similar to our findings. Similarly [31], concluded that the RMS delay spread is significantly influenced by the local environment of the Tx and Rx antennas.

3.6 Spatial Aliasing

Virtual antenna arrays do not have the problem of mutual coupling found in real antenna arrays, however, when the inter-element distance is greater than 0.5λ there is spatial aliasing resulting in grating lobes. Grating lobes cause an ambiguity in the AOA estimation.

When designing virtual antenna arrays for channel measurements, the spatial aliasing problem needs to be considered carefully. For some incident angles $[0, 90, 180, 270, 360]^\circ$ the grating lobes can have a high peak with a power difference of close to 2 dB from the main lobe.

For the ULA an inter-element spacing of 0.5λ solves this problem. However for the URA, grating lobes can be seen for an inter-element spacing of 0.5λ . This is because the distance between the diagonal elements is greater than 0.5λ . To solve this problem and reduce the power of the grating lobe significantly by about 26 dB we need to have an inter-element spacing of 0.4λ between the adjacent elements.

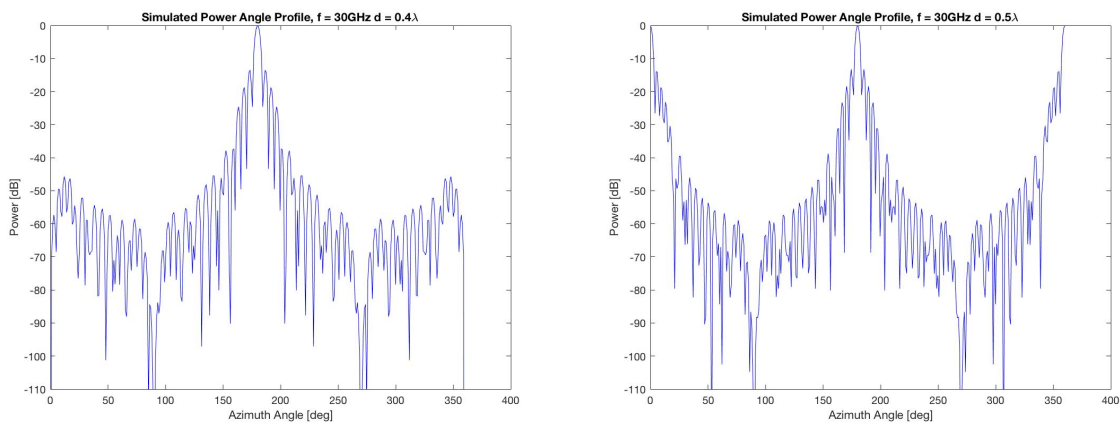
3.6.1 Simulated Response

The antenna response was simulated before the measurement campaign to avoid the grating lobe problem or to keep the sidelobe level minimum. The simulated responses were done for a URA of the same configuration as the measurement set up. The inter-element spacing used in the simulation were 0.4λ and 0.5λ .

The simulation was carried out for an incident ray at 30 GHz, with a power of 0 dB and an incident angle of 180° . This was similar to our measurement setup where the LOS component had an incident angle of 180° . The effects of spatial aliasing are as shown in fig. 3.6b. Fig. 3.6a shows that grating lobes are eliminated by using an inter-element spacing of 0.4λ .

3.6.2 Grating Lobes in Measurements

As shown in simulation results fig. 3.6, grating lobes in measurement data can be a stumbling block in accurately characterizing the propagation channel. As noted in the simulation, grating lobes are very severe for the incident angles $[0, 90, 180, 270, 360]^\circ$. This results in obscuring weaker paths at these angles. This is problematic especially for the LOS scenario. Since the LOS component is at 180° , the grating lobes are quite significant. The effect of the grating lobes is more severe in the elevation angle



(a) Simulated Power Angle Profile with $d = 0.4\lambda$.

(b) Simulated Power Angle Profile with $d = 0.5\lambda$.

Fig. 3.6: Simulated Antenna Array Response.

estimation, since the fictitious angles are super-imposed on paths that could be weaker but nonetheless significant.

For example in this measurement campaign when the incident angle for the direct path for LOS, is at 180° , there is a back reflection from the wall at 0° , but after multiple reflections from the wall, it becomes difficult to distinguish between the fictitious angles and the actual angles.

The grating lobes are illustrated in fig. 3.4c for measurement campaign 1. In the OLOS scenario, grating lobes were not noticeable as shown in fig. 3.4d since the specular components were not at incident angles outlined in section 3.6.1.

In measurement campaign 2, the spatial aliasing problem is solved by using an inter-element spacing of 0.4λ . As shown in fig. 3.4a, grating lobes for the LOS component are kept at a power level of less than 30 dB from the main peak.

CONCLUSION AND FUTURE WORK

4.1 Conclusion

The channel sounding setup was robust and highly repeatable as demonstrated in the phase variation test. The magnitude variation was 0.1 dB on all the vertices for the entire frequency range and the phase variation was 2.5° which indicates a high reliability and repeatability. The repeatability was also shown in the angle estimation for the two measurement campaigns which had a lot of similarities with the difference being due changes in the room furnishing and the relative positions of the antennas.

It was demonstrated experimentally the effect of the wall reflectivity on the RMS delay spread. In calculating the RMS delay spread, the delay bins to be included in the calculation vary from system to system and the criterion is governed by the dynamic range.

It was further demonstrated, experimentally the importance of the LOS component in millimeter wave communication as has been proposed in literature.

The virtual UCuA radiation pattern acts as a spatial filter, thus some paths that could have been from the floor or ceiling were not detected in the elevation angle estimation.

4.2 Future Work

In massive MIMO, there has been an interest to investigate how close can users be to safely assume that the channels are uncorrelated, or in other words the spatial separation of users. The co-location measurement in this thesis was carried out for this purpose. The Tx antenna is considered as the BS and the two antennas in this set up are considered the MS.

A question that was raised in [32] on whether all antenna elements contribute equally. As shown in 3.1, some scatterers are not seen by some antenna elements. This can be used as a basis of a study on antenna selection in massive MIMO similar to the study in [32].

In future work it would be intuitive to extend the measurement setup to have more antennas as well as adopt the measurement system in [7], in order to have a higher dynamic range. The VNA, (PNA N5772A) has 4 ports, with an option of adding an extra port. This would allow for an additional 2 antennas to be installed in future measurements.

Since the measurement was carried out in a wide bandwidth 26 -30 GHz, the beam pattern of the array is frequency variant and this causes high sidelobe levels thus resulting in the weak paths being buried in the sidelobes [11]. This can be solved by using sidelobe suppression techniques like Dolph-Chebyshev weighting for uniform arrays in [17]. We intend to apply these techniques to the data collected as well as develop improved angle detection algorithms.

In the OLOS scenario as shown in fig. 3.4b, it can be quite difficult to analyse individual paths. This would be the same case in a LOS scenario for richly furnished rooms or laboratory environments where many specular reflectors exist. This leads to the need of an analysis of MPC using cluster models [33]. Existing models include the COST 2100 MIMO model [34].

From the results, we have seen that the tail of the PDP changes with a change in furniture. A detailed study of the decay rate will be carried out to augment the existing research for instance in [35]. To get a conclusive result measurements need to be carried out in different rooms of different sizes and material composition, which was beyond the scope of this thesis.

Finally having performed measurement campaigns at the center frequency 28 GHz, we would like to extend the measurement campaigns to other millimeter wave bands for comparison with this analysis.

BIBLIOGRAPHY

- [1] J. G. Andrews, S. Buzzi, W. Choi, S. V. Hanly, A. Lozano, A. C. K. Soong, and J. C. Zhang, “What will 5g be?” *IEEE Journal on Selected Areas in Communications*, vol. 32, no. 6, pp. 1065–1082, June 2014.
- [2] G. R. Maccartney, T. S. Rappaport, S. Sun, and S. Deng, “Indoor office wideband millimeter-wave propagation measurements and channel models at 28 and 73 ghz for ultra-dense 5g wireless networks,” *IEEE Access*, vol. 3, pp. 2388–2424, 2015.
- [3] T. S. Rappaport, S. Sun, R. Mayzus, H. Zhao, Y. Azar, K. Wang, G. N. Wong, J. K. Schulz, M. Samimi, and F. Gutierrez, “Millimeter wave mobile communications for 5g cellular: It will work!” *IEEE Access*, vol. 1, pp. 335–349, 2013.
- [4] W. Fan, I. Llorente, J. Nielsen, K. Olesen, and G. Pedersen, “Measured wideband characteristics of indoor channels at centimetric and millimetric bands,” *EURASIP Journal on Wireless Communications and Networking*, vol. 2016, no. 58, 2016, special issue on Radio Channel models for higher frequency bands.
- [5] S. Ranvier, M. Kyro, K. Haneda, T. Mustonen, C. Icheln, and P. Vainikainen, “Vna-based wideband 60 ghz mimo channel sounder with 3-d arrays,” in *2009 IEEE Radio and Wireless Symposium*, Jan 2009, pp. 308–311.
- [6] A. M. Street, L. Lukama, and D. J. Edwards, “Use of vnas for wideband propagation measurements,” *IEE Proceedings - Communications*, vol. 148, no. 6, pp. 411–415, Dec 2001.
- [7] J. Hejselbaek, W. Fan, and G. F. Pedersen, “Ultrawideband vna based channel sounding system for centimetre and millimetre wave bands,” in *2016 IEEE 27th Annual International Symposium on Personal, Indoor, and Mobile Radio Communications (PIMRC)*, Sept 2016, pp. 1–6.
- [8] RUSK Channel Sounder. [Online]. Available: <http://www.channelsounder.de/welcome.html>
- [9] V. Degli-Esposti, F. Fuschini, E. M. Vitucci, M. Barbiroli, M. Zoli, L. Tian, X. Yin, D. A. Dupleich, R. Müller, C. Schneider, and R. S. Thomä, “Ray-tracing-based mm-wave beamforming assessment,” *IEEE Access*, vol. 2, pp. 1314–1325, 2014.
- [10] J. Medbo, H. Asplund, and J. E. Berg, “60 ghz channel directional characterization using extreme size virtual antenna array,” in *2015 IEEE 26th Annual International Symposium on Personal, Indoor, and Mobile Radio Communications (PIMRC)*, Aug 2015, pp. 176–180.
- [11] I. Llorente, W. Fan, and G. Pedersen, *A frequency invariant beamformer for channel parameter estimation in millimeter wave bands*. United States: IEEE, 11 2015.
- [12] C. Gentile, A. J. Braga, and A. Kik, “A comprehensive evaluation of joint range and angle estimation in ultra-wideband location systems for indoors,” in *2008 IEEE International Conference on Communications*, May 2008, pp. 4219–4225.

-
- [13] C. Gentile, S. M. Lopez, and A. Kik, "A comprehensive spatial-temporal channel propagation model for the ultra-wideband spectrum 2-8 ghz," in *GLOBECOM 2009 - 2009 IEEE Global Telecommunications Conference*, Nov 2009, pp. 1–6.
- [14] Z. Chen, G. Gokeda, and Y. Yu, *Introduction to Direction-of-Arrival Estimation*, ser. Artech House signal processing library. Artech House, 2010.
- [15] C. Gustafson, F. Tufvesson, S. Wyne, K. Haneda, and A. F. Molisch, "Directional analysis of measured 60 ghz indoor radio channels using sage," in *2011 IEEE 73rd Vehicular Technology Conference (VTC Spring)*, May 2011, pp. 1–5.
- [16] F. Zhang, W. Fan, and G. F. Pedersen, "Analytic and experimental investigation of beamforming algorithms for mm-wave channel characterization," in *2017 11th European Conference on Antennas and Propagation (EUCAP)*, March 2017, pp. 146–150.
- [17] —, "Channel characterization using large scale uniform arrays with sidelobe suppression," in *2017 11th European Conference on Antennas and Propagation (EUCAP)*, March 2017, pp. 3190–3194.
- [18] P. F. M. Smulders and L. M. Correia, "Characterisation of propagation in 60 ghz radio channels," *Electronics Communication Engineering Journal*, vol. 9, no. 2, pp. 73–80, Apr 1997.
- [19] S. Geng, J. Kivinen, X. Zhao, and P. Vainikainen, "Millimeter-wave propagation channel characterization for short-range wireless communications," *IEEE Transactions on Vehicular Technology*, vol. 58, no. 1, pp. 3–13, Jan 2009.
- [20] S. Zhekov, A. Tatomirescu, and G. Pedersen, "Antenna for ultrawideband channel sounding," *IEEE Antennas and Wireless Propagation Letters*, pp. 692–695, 2016.
- [21] S. S. Zhekov, A. Tatomirescu, and G. F. Pedersen, "Modified biconical antenna for ultrawideband applications," in *2016 10th European Conference on Antennas and Propagation (EuCAP)*, April 2016, pp. 1–5.
- [22] A-INFO SZ-2003000/P. [Online]. Available: http://www.ainfoinc.com/en/pro_pdf/new_products/antenna/Bi-Conical%20Antenna/tr_SZ-2003000-P.pdf
- [23] P. Pagani, F. T. Talom, P. Pajusco, B. Uguen, and P. N. Favennec, *Ultra Wide Band Radio Propagation Channel*. Wiley, 2008.
- [24] *Operating Manual MP 35E*, M-400 Series Linear Positioning Stages, Physik Instrumente, 25 October 1999.
- [25] *Operating Manual MS 52E*, C-844 Precision DC-Motor Controller, Physik Instrumente, 30 August 2000.
- [26] Pyvisa: Control your instruments with python. [Online]. Available: <https://pyvisa.readthedocs.io/en/stable/>
- [27] L. C. Godara, "Application of antenna arrays to mobile communications. ii. beam-forming and direction-of-arrival considerations," *Proceedings of the IEEE*, vol. 85, no. 8, pp. 1195–1245, Aug 1997.
- [28] M. Jacob, S. Priebe, R. Dickhoff, T. Kleine-Ostmann, T. Schrader, and T. Kurner, "Diffraction in mm and sub-mm wave indoor propagation channels," *IEEE Transactions on Microwave Theory and Techniques*, vol. 60, no. 3, pp. 833–844, March 2012.

- [29] T. Manabe, Y. Miura, and T. Ihara, "Effects of antenna directivity and polarization on indoor multipath propagation characteristics at 60 ghz," *IEEE Journal on Selected Areas in Communications*, vol. 14, no. 3, pp. 441–448, Apr 1996.
- [30] K. Haneda, J. Järveläinen, A. Karttunen, M. Kyrö, and J. Putkonen, "Indoor short-range radio propagation measurements at 60 and 70 ghz," in *The 8th European Conference on Antennas and Propagation (EuCAP 2014)*, April 2014, pp. 634–638.
- [31] A. A. M. Saleh and R. Valenzuela, "A statistical model for indoor multipath propagation," *IEEE Journal on Selected Areas in Communications*, vol. 5, no. 2, pp. 128–137, February 1987.
- [32] X. Gao, O. Edfors, F. Tufvesson, and E. G. Larsson, "Massive mimo in real propagation environments: Do all antennas contribute equally?" *IEEE Transactions on Communications*, vol. 63, no. 11, pp. 3917–3928, Nov 2015.
- [33] X. Gao, "Doctoral Thesis: Massive MIMO in Real Propagation Environments," 2016-01-26. [Online]. Available: <http://portal.research.lu.se/ws/files/3820621/8569798.pdf>
- [34] X. Gao, F. Tufvesson, and O. Edfors, "Massive mimo channels ; measurements and models," in *2013 Asilomar Conference on Signals, Systems and Computers*, Nov 2013, pp. 280–284.
- [35] G. Steinböck, T. Pedersen, B. H. Fleury, W. Wang, and R. Raulefs, "Experimental validation of the reverberation effect in room electromagnetics," *IEEE Transactions on Antennas and Propagation*, vol. 63, no. 5, pp. 2041–2053, May 2015.